Chemical Engineering Journal 500 (2024) 156923

Contents lists available at ScienceDirect

Chemical Engineering Journal

journal homepage: www.elsevier.com/locate/cej

Tumor microenvironment-based smart beacon drug delivery system for *in situ* visualization of tumor therapy

Yongchun Wei [a], Jiaqi Xing [a], Jiarao Sun [a], Wei Chen [a], Gongchang Yu [b], Bin Shi [b,*], Xintian Shao [c,*], Yanfeng Wang [a,*]

[a] School of Pharmaceutical Sciences & Institute of Materia Medica, Shandong First Medical University & Shandong Academy of Medical Sciences, National Key Laboratory of Advanced Drug Delivery System, Key Laboratory for Biotechnology Drugs of National Health Commission (Shandong Academy of Medical Sciences), Key Lab for Rare & Uncommon Diseases of Shandong Province, Jinan 250117, Shandong, China

[b] Department of Traditional Chinese Medicine Orthopedics, Neck-Shoulder and Lumbocrural Pain Hospital of Shandong First Medical University, Shandong First Medical University & Shandong Academy of Medical Sciences, Jinan 250062, Shandong, China

[c] School of Life Sciences, Medical Science and Technology Innovation Center, Shandong First Medical University & Shandong Academy of Medical Sciences, Jinan 250117, China

ARTICLE INFO

Keywords:
Beacon drug
Heme oxygenase 1
Anti-tumor
Super-resolution imaging

ABSTRACT

Real-time monitoring of the effectiveness of tumor-targeted drugs is crucial for assessing their impact. To address this need, we developed a beacon drug delivery system, MDB, which incorporates tumor targeting, anti-tumor effects, and near-infrared fluorescence emission for on-site visualization of tumor therapy. In non-cancerous cells, MDB remains inactive as a prodrug but is selectively activated within tumor cells when the borate ester group reacts with H_2O_2 in the tumor microenvironment (TME), releasing the beacon drug MDBRe. MDBRe can down-regulate the expression of the protein heme oxygenase 1 (HO-1), ultimately disrupting the mitochondrial energy supply system and leading to tumor cell death. It also emits near-infrared fluorescence for drug tracking under structured illumination microscopy (SIM). Both *in vitro* and *in vivo* experiments confirm the effective delivery of MDBRe by MDB to H_2O_2-enriched tumor tissues, resulting in a potent anti-tumor effect, visualization of drug distribution in tumors, and monitoring of therapy progress. In conclusion, our approach presents a novel method for targeted drug delivery to tumors and enables real-time visual monitoring of the treatment process.

1. Introduction

Cancer remains a significant global health challenge, causing millions of deaths annually. A crucial therapeutic strategy involves developing drugs that can precisely target key subcellular organelles or essential proteins that regulate tumor growth and metastasis [1–3]. Targeted drugs achieve this precision by binding highly specifically to molecular targets on tumor cells, thereby inhibiting key signaling pathways necessary for tumor growth and survival. For instance, heme oxygenase-1 (HO-1) is an enzyme known for its anti-inflammatory, antioxidant, and anti-apoptotic properties [4–7]. Targeted inhibition of HO-1 has been shown to suppress the survival and metastasis of tumor cells [8–10], but current inhibitors lack the ability to distinguish between tumor and normal tissues [11–13]. To address this limitation, a common strategy involves delivering drugs that specifically target the tumor microenvironment (TME) [14–16]. Hydrogen peroxide (H_2O_2) is a prevalent reactive oxygen species (ROS) molecule in the TME and can be utilized as a molecular target to facilitate the precise release of drugs within the tumor region, thereby minimizing damage to normal tissues [17,18]. Current efforts in developing targeted drugs focus primarily on small molecule compounds with molecular weights of 500 Da [19,20]. However, for safety considerations, these drugs must bind specifically to their designated targets with minimal off-target effects. Thus, evaluating drug accumulation at the target site and its specific binding to the target are critical aspects of drug assessment.

In-situ drug visual monitoring technology provides a straightforward and efficient method for detecting drug-target binding, especially with the improved spatial resolution of up to 100 nm achieved through super-resolution microscopy imaging techniques like structured illumination microscopy (SIM) [21,22]. This advancement paves the way for investigating drug distribution and metabolism at the subcellular level [23,24]. However, the introduction of fluorophore modifications can

* Corresponding authors.
E-mail addresses: bshi@sdfmu.edu.cn (B. Shi), shaoxintian@sdfmu.edu.cn (X. Shao), wangyanfeng@sdfmu.edu.cn (Y. Wang).

https://doi.org/10.1016/j.cej.2024.156923
Received 26 July 2024; Received in revised form 21 September 2024; Accepted 18 October 2024
Available online 20 October 2024

potentially alter the binding affinity of drugs to their targets, leading to potential misunderstandings regarding the actual behavior of the drug within cells [25,26]. Furthermore, relying on fluorescence-based signal readouts may produce "false positives" with fluorophore-like drug molecules [27], causing them to be erroneously excluded from large-scale drug screening endeavors. Consequently, the direct visualization of drugs within cells remains a lingering challenge in current technologies.

To address this issue, we propose a novel visual beacon drug delivery strategy that combines tumor microenvironment (TME) responsiveness, therapeutic drug release, and visualized therapy within a single molecule. In this molecular design, 2-(3-(4-hydroxystyryl)-5,5-dimethylcyclohex-2-enylidene) malononitrile (MDBRe) serves as a beacon drug with visual therapeutic capabilities. The boronate ester group acts as a TME-sensitive site responsive to H_2O_2, also functioning as a fluorescent protection group for MDBRe, which suppresses its fluorescence emission. Experimental findings revealed that the prodrug MDB remains stable in normal tissue cells, exhibiting no therapeutic nor fluorescence activity. When situated in tumor cells with elevated levels of H_2O_2, MDB rapidly releases the active beacon drug MDBRe. Notably, MDBRe was observed to interact with HO-1 under SIM, a pivotal factor in tumor cell proliferation and survival [28–30]. It effectively disrupted the mitochondrial energy supply system of tumor cells by reducing HO-1 levels, inducing mitochondrial dysfunction, and consequently impeding tumor growth.

2. Experimental section

2.1. General materials and instrument

General methods were used unless otherwise stated; Chemical materials and solvents in this work were of analytical grades and used without further purification (The purity of chemicals was over 95 %, and the purity of solvents was over 99.9 %). All solutions of various reactive oxygen species (ROS) and reactive nitrogen species (RNS) were prepared using double distilled water. Dulbecco's modified Eagle's medium (DMEM) phenol-free medium, and fetal bovine serum (FBS) were purchased from VivaCell, Shanghai, China. Biological reagents and protein samples were purchased from Servicebio, Wuhan, China. Confocal glass-bottom culture dishes were purchased from SAINING Biotechnology. High-resolution mass Spectrometries (HRMS) of the compounds were measured by electrospray ionization (ESI) equipped with Agilent 1290LC-6540. Absorption spectra were recorded using a UV-3600 plus spectrometer (Shimadzu). Fluorescence spectra were characterized on an F-7100 fluorescence spectrophotometer (Hita-chi). The pH measurements were carried out with a pH acidometer (PHS-3C). The super-resolution imaging of mitochondria was taken using OMX 3D-SIM microscope (Delta Vision, Inc., Issaquah, WA, USA). The intravital fluorescence images of mice were acquired by the IVIS Lumina Series III from PerkinElmer. The images of mitochondrial morphology were captured by transmission electron microscopy (Hita-chi TEM system). The fluorescence images of Tunel and immunofluorescence were acquired through a confocal fluorescence microscope (Olympus FLUOVIEW FV3000). Protein bands are obtained by Azure Biosystems, Inc (Model c400).

2.2. Molecular docking simulation

The flat structure of the MDBRe was drawn and converted to the 3D structure by ChemBio3D Ultra 14.0 software. The 3D structure of HO-1 (PDB Code: 1IRM) was downloaded from RCSB Protein Data Bank (https://www.rcsb.org). Protein HO-1 was processed by Maestro of Schrodinger 2018, and the protein processing operation used default parameters. The search grid of the HO-1 site was identified as center_x: 4.618, center_y: −20.196, and center_z: 3.001 with dimensions size_x: 13.6, size_y: 14.9, and size_z:18.0. The XP (extra precision) mode docking was processed through Glide of Schrodinger, and the default parameters were used if it was not mentioned. The docking results were exported to PDB format, and the 3D analysis of the combined mode was chosen and performed using PyMol 2.4.1 software (https://www.pymol.org). The 2D interaction mode is visualized by Maestro.

2.3. Synthesis and characterization

Mitochondrial-targeted prodrug (MDB) in Scheme S1 was synthesized according to the following method. A 0.406 mmol (117.7 mg) amount of MDBRe, 0.452 mmol (134.1 mg) of 4−(Bromomethyl) benzeneboronic acid pinacol ester, 0.92 mmol (127.1 mg) of K_2CO_3 were dissolved in dried $CNCH_3$. The mixture was stirred for 4 h at 60 °C, and then the solvent was removed under vacuum. The resultant was further purified by silica gel column chromatography (DCM/PE = 20:3, *V/V*) to give MDB, a yellow solid, 140.3 mg with a yield: 68.3 %. ^{1}H NMR (500 MHz, DMSO-d_6) δ 7.71–7.59 (m, 4H), 7.44 (d, J = 7.6 Hz, 2H), 7.24 (d, J = 3.1 Hz, 2H), 7.08–6.97 (m, 2H), 6.81 (s, 1H), 5.18 (s, 2H), 2.58 (s, 2H), 2.51 (s, 2H), 1.27 (s, 12H), 0.99 (s, 6H). ^{13}C NMR (126 MHz, DMSO) δ 170.35, 159.55, 156.41, 140.18, 137.57, 134.58, 129.61, 128.95, 127.43, 126.85, 121.89, 115.34, 113.21, 83.69, 75.38, 69.12, 42.33, 38.20, 31.68, 30.27, 27.44, 24.67. HRMS: *m/z* $[M+Na]^+$ calcd for 529.2741, found 529.2653. The synthesis steps and characterization results of other intermediates are in the supporting information (Figs. S1–S7).

2.4. MST measurements

The stock solution concentration of MDBRe is 1 mM. Protein HO-1 solution with a concentration of 11 μM was stored at −20 °C. This stock solution was used for the preparation of a 16-step serial dilution in PBST buffer. The series of protein HO-1 concentrations are 2.75 μM, 0.688 μM, 0.172 μM, 0.0859 μM, 0.0215 μM, and 0.00269 μM. Then 10 μL of 1 mM MDBRe was added to all 16 vials and samples were mixed by pipetting up and down. Reactions were incubated for 30 min at room temperature away from light and then loaded into Capillaries. The binding of MDBRe to HO-1 is characterized by Kd.

2.5. Spectrometric studies

Prodrug MDB was dissolved in dimethyl sulfoxide (DMSO) to get a stock solution. The measured solutions were diluted with PBS/DMSO = 1/1, *V/V*, 10 mM, pH = 7.4, to a final concentration of 10 μM. Various reactive oxygen species (ROS) and reactive nitrogen species (RNS) including H_2O_2, •OH, NO_2^-, ClO^-, NO_3^-, $^1O_2$, $ONOO^-$, NO, t-$BuOO^-$ were prepared according to the literature methods [31]. The final concentration of ROS and RNS is 100 μM.

2.6. Cytotoxicity assay

To determine the biocompatibility of MDB against different cell types, HeLa, AT3, H9c2, and L929 cells were seeded in the 96-well plate with 8×10^3 cells per well and incubated for 12 h in DMEM. The cells were washed with PBS once and then incubated in fresh DMEM containing various amounts of MDB (0, 10, 20, 30 μM) for 24 h respectively. Then, 10 μL CCK-8 was added to each well and incubated at 37 °C under 5 % CO_2 for 2 h. The absorption wavelength was measured by an enzyme labeling apparatus (Synergy HT) at 450 nm. The cell viability (%) was calculated according to the following equation: Cell viability (%) = (mean of absorbance value of the treatment group) / (mean of absorbance value of the control group).

2.7. Cell culture and treatment

Various types of cells were cultured in DMEM supplemented with 10 % FBS, 1 % penicillin, and 1 % streptomycin in a 5 % CO_2 humidified

incubator at 37 °C. The cells were incubated with MDB/MDBRe (10 μM) at 37 °C for 60 min in fresh DMEM, further co-incubated with PK Mito-Tracker Deep Red (PKMTDR) at 37 °C for 30 min, washed three times with PBS buffer, finally, cells were cultured in phenol-free medium and observed.

2.8. OMX 3D-SIM super-resolution microscope imaging

Various types of cells were cultured on 35 mm glass-bottom culture dishes and observed under an OMX 3D-SIM super-resolution microscope (Delta Vision, Inc., Issaquah, WA, USA) equipped with a 60×/1.42 numerical aperture oil-immersion objective lens and solid-state lasers. MDBRe was excited at 561 nm and emitted at 660–670 nm. Captured SIM images were analyzed by the software of ImageJ equipped with a fluorescence intensity measurement tool.

2.9. Animal experiment

The animal experiment protocol had been approved by the Institutional Animal Care and Use Committee: Twenty BALB/c nude Crli female mice (about 4-week-old) were purchased from the Vital River Laboratory Animal Technology Co., Ltd., Beijing, China. The tumor xenografts were induced by subcutaneously inoculating HeLa cells (1×10^6/100 μL) into the right flank region. Tumor size and weight were measured at the endpoint of the experiment, and tumor volume was calculated by the following formula: $V = ab^2/2$ (a and b represent the long and short diameters, respectively). Finally, the tumor size and weight were compared by using statistical analysis.

2.10. Blood compatibility test

The blood compatibility of MDBRe was evaluated by hemolysis. A total of 2 mL of fresh mice blood was obtained through the eyes. Subsequently, the obtained blood was centrifuged (1500 × g, 5 min) and washed 3 times with PBS. Then, 500 μL concentration of 10 % red blood cells was exposed to 500 μL of Triton X-100, PBS, 10, 20, 30, 40, and 50 μM MDBRe. After incubation at 37 °C for 60 min, centrifugation (2500 × g, 5 min) was performed again. Finally, the OD value of the supernatant at 540 nm was measured by the microplate reader. The positive control was 0.1 % Triton X-100 and the negative control was PBS. The formula for calculating the hemolysis ratio is as follows:

$$Hemolysisratio(\%) = \frac{OD(Sample) - OD(PBS)}{OD(Triton) - OD(PBS)} \times 100\%$$

2.11. Apoptosis detection

Tumor tissue was sliced and the *in situ* apoptosis of the tumors was evaluated by using a terminal-deoxynucleotidyl transferase-mediated dUTP-biotin nick end labeling (TUNEL) staining. Three groups were set up in the apoptosis experiment, namely positive, control, and experimental groups (MDB-treated). Tissue sections were finally mounted with neutral balsam (Shanghai Macklin Biochemical Co., Ltd). Apoptosis imaging was observed under a confocal fluorescence microscope (Olympus FLUOVIEW FV3000).

2.12. Flow cytometry analysis

In order to study the apoptosis of the cells treaded by MDB, HeLa cells were stained with Annexin-EGFP/PI. Firstly, HeLa cells were seeded in DMEM supplemented with 10 % FBS at 37 °C for 24 h. Then the medium culture was replaced with fresh medium containing 0, 10, 20, and 30 μM of MDB. After being treated with MDB for 24h, the cells were digested by trypsin without EDTA and washed three times with precooled PBS, and cells were resuspended in Binding Buffer and incubated with Annexinv-EGFP/PI. Finally, a total of 10,000 cells per sample were collected with an Cytometer (FongCyte™).

2.13. Proteomic analysis

In the experimental group, HeLa cells were incubated with MDB (10 μM) for 1 h in DMEM supplemented with 10 % FBS and washed with fresh DMEM five times. The control group did not do any treatment. Cells from the experimental group and the control group were collected separately by using a spatula. Samples were sonicated three times on ice using a high-intensity ultrasonic processor (Scientz) in lysis buffer (8 M urea, 1 % protease inhibitor cocktail). The remaining debris was removed by centrifugation at 12,000 g at 4 °C for 10 min. Finally, the supernatant was collected and the protein concentration was determined with a BCA kit according to the manufacturer's instructions. The separated peptides were analyzed in Q Exactive™ HF-X (ThermoFisher Scientific) with a nano-electrospray ion source. Mass spectral data were retrieved using Maxquant (v1.6.15.0). Retrieval parameter settings: the database is Homo_sapiens_9606_SP_20210721.fasta (20387 sequences). Trypsin/P was specified as a cleavage enzyme allowing up to 2 missing cleavages. The mass tolerance for precursor ions was set as 20 ppm in the first search and 5 ppm in the main search, and the mass tolerance for fragment ions was set as 0.02 Da. Carbamidomethyl on Cys was specified as a fixed modification, and acetylation on protein N-terminal and oxidation on Met were specified as variable modifications. FDR was adjusted to <1 %. Gene Ontology (GO) annotation proteome was derived from the UniProt-GOA database (http://www.ebi.ac.uk/GOA/). The GO with a corrected p-value < 0.05 is considered significant. Proteomic Analysis was provided by Jingjie PTM BioLab (Hangzhou). Co. Inc.

2.14. Western-blot assay

We had prepared whole tissue lysate for Western blotting. Broken tissue homogenate was lysed using a radioimmune precipitation assay (RIPA) buffer for 30 min on ice. After treatment, the lysates were centrifuged at 15,000 rpm at 4 °C and the supernatant was collected. The protein concentration of each sample was tested using a BCA protein assay reagent kit. Equal protein masses (50 μg) of whole tissue lysate were resolved on SDS-polyacrylamide gel electrophoresis and transferred to PVDF membranes in an ice bath. The primary antibody was incubated at 4 °C for 12 h, and the secondary antibody was incubated at room temperature for 2 h. GAPDH and ß-tubulin were used as controls. COX-2 antibody (Catalog# ET1610-23) was purchased from HUABIO.

2.15. Data analysis

The data were processed using GraphPad Prism and Origin 2018. The quantitative data analysis was presented as mean ± standard error of the mean (SEM). Sample sizes in all graphs are indicated in the corresponding figure legends. The P values < 0.05 were considered statistically significant (*P < 0.05, **P < 0.01, ***P < 0.001).

3. Results and discussion

3.1. Beacon drug delivery system design and initial characterization

To develop a visualization beacon drug delivery system, dicyanoisophorone was chosen as the fluorophore due to its excellent spectroscopic properties and stable absorption characteristics. Subsequently, *p*-hydroxybenzene was conjugated to dicyanoisopherone to create the beacon drug MDBRe (Fig. 1a). The *p*-hydroxybenzene moiety served as a module for binding to HO-1 [32], its inclusion not only increased the affinity of the beacon drug for HO-1 but also enhanced its visualization ability by extending the conjugate system. To ensure precise delivery of the beacon drug MDBRe to the tumor site, borate ester groups were added to the MDBRe structure (Fig. S1). These groups are activated by

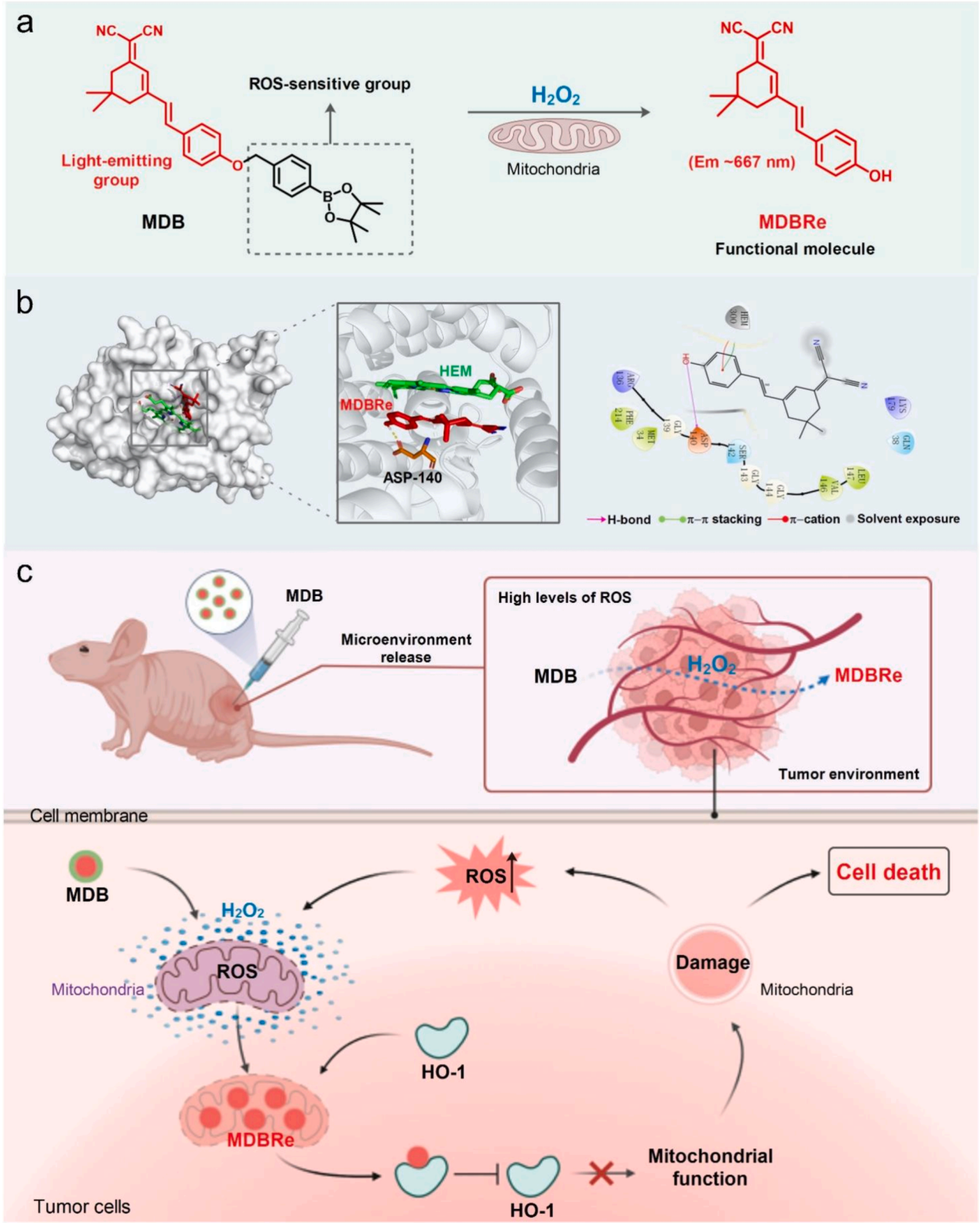

Fig.1. Schematic diagram for the H_2O_2-activated prodrug MDB and the application *in vivo* therapy. a Chemical structure of H_2O_2-responsive prodrug MDB. b Docked poses of MDBRe (red) and HO-1 and plan view of drug molecule MDBRe interacting with HO-1. The search grid of the HO-1 site was identified as center_x: 4.618, center_y: −20.196, and center_z: 3.001 with dimensions size_x: 13.6, size_y: 14.9, and size_z:18.0. c Schematic illustration of the anticancer mechanism of MDB in the tumor. (For interpretation of the references to colour in this figure legend, the reader is referred to the web version of this article.)

the high concentrations of H_2O_2 within the TME (ranging from 100 × 10^{-6} M to 1 × 10^{-3} M) [33], allowing selective release of MDBRe at the tumor site, thereby exerting its therapeutic effect while minimizing damage to normal tissues. Additionally, the presence of borate ester groups renders the prodrug MDB devoid of biological activity and fluorescence. The fluorescence signal becomes detectable only upon the release of MDBRe in response to H_2O_2. This transition from "fluorescence off" to "fluorescence on" serves as a crucial indicator for beacon drug delivery and the treatment of tumor sites (Fig. 1b and c).

To confirm the responsiveness of MDB to H_2O_2, H_2O_2 (100 μM) was introduced into the MDB solution in PBS buffer (10 mM, pH = 7.4). Upon H_2O_2 addition, a new absorption peak at 561 nm emerged in the UV–vis spectrum (Fig. S8) alongside a significant increase in fluorescence emission at 667 nm (λex = 561 nm) (Fig. 2c). The fluorescence intensity exhibited a gradual rise with the incremental addition of H_2O_2 (0–90 μM) (Fig. 2c), displaying a strong linear relationship (R^2 = 0.9894) (Fig. S9). The detection limit of H_2O_2 by MDB was determined to be 392 nM using the formula LOD = 3σ/k (σ is the standard deviation of the blank, k is the slope of fluorescence intensity and H_2O_2 concentration) [34]. To validate the selectivity of MDB for H_2O_2, fluorescence spectra were examined in the presence of other ROS and reactive nitrogen species (RNS) [35,36]. It was found that none of the bioactive species, except H_2O_2, elicited the enhanced fluorescence signal of MDB (Fig. S10), indicating that H_2O_2 was the sole physiological species capable of efficiently activating MDB.

Furthermore, we assessed the impact of incubation time and pH on MDB activation. The findings indicated that the fluorescence intensity of MDB reached its peak at 210 min and maintained stability thereafter (Fig. S11). Additionally, MDB exhibited optimal activation properties at physiological pH (pH = 7.4) (Fig. S12). Thus, MDB demonstrated the ability to be selectively activated by H_2O_2 under physiological conditions, suggesting its potential for future applications in live cell imaging. To further confirm the formation of MDBRe as the activation product, we compared the fluorescence spectra of MDB in the presence of H_2O_2 with that of MDBRe, showing a significant overlap between them (Fig. S13). High-resolution mass spectrometry data further supported the generation of MDBRe (Fig. S14), indicating that MDB can be activated in the presence of elevated H_2O_2 levels in the TME, releasing the active drug MDBRe.

Subsequently, we investigated the binding mode of MDBRe with HO-1 through molecular docking techniques. The X-ray crystal structure of HO-1 (PDB code 1IRM) was utilized as a reference model for studying the protein structure. Our findings indicated that the hydroxyl group of MDBRe forms a hydrogen bond with the ASP-140 residue of HO-1 in a favorable binding orientation (Fig. 1b). ASP-140 residues are crucial for the catalytic activity and normal biological function of HO-1 [32],

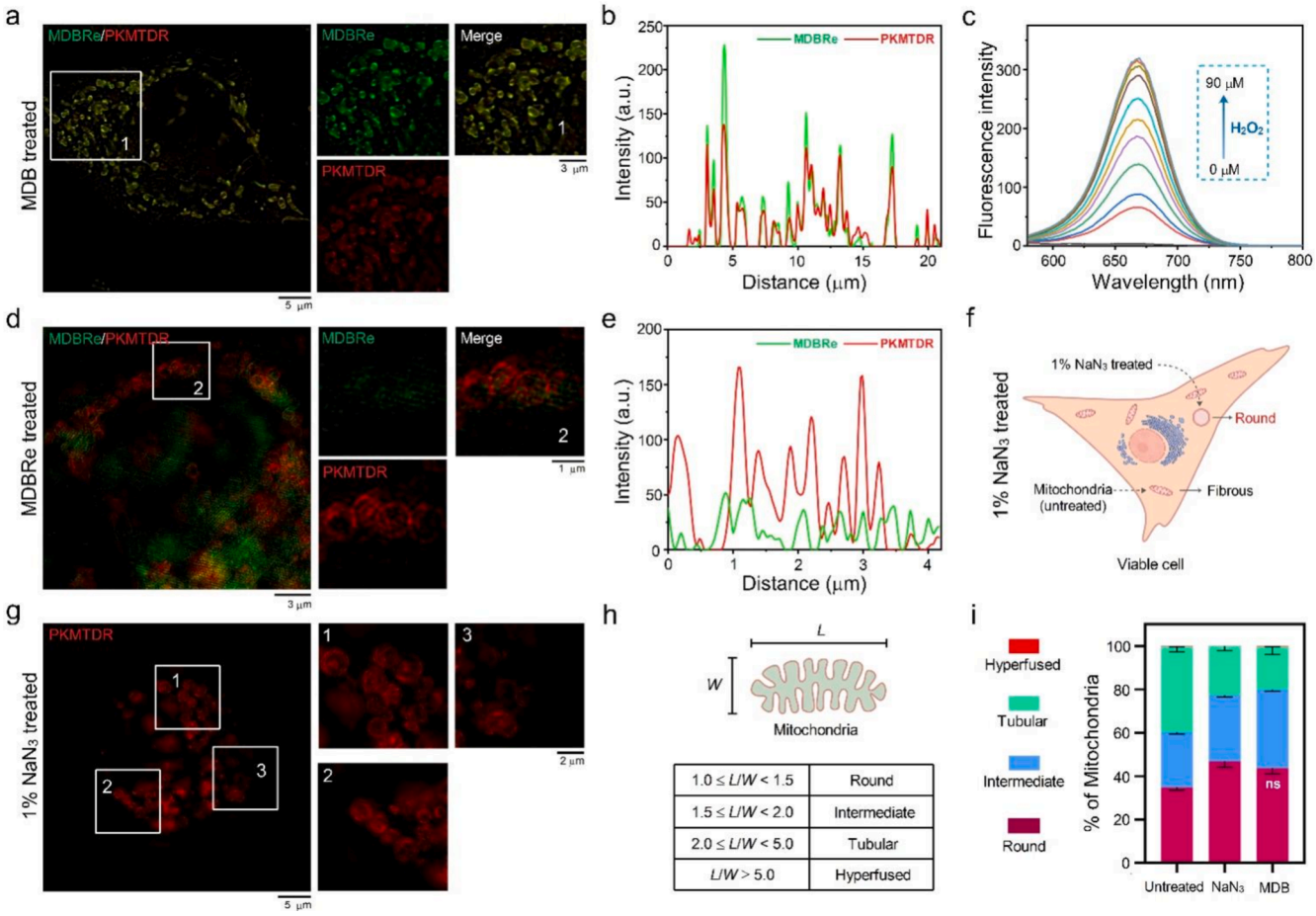

Fig.2. Characterization of prodrug MDB in HeLa cells via SIM imaging. a SIM images of HeLa cells stained with MDB (10 μM) for 1 h. b Representative fluorescence intensity of MDBRe (green line) and PKMTDR (red line) in the mitochondrial region. MDBRe, green, λex = 561 nm; PKMTDR, red, λex = 640 nm. c Fluorescent spectral changes of MDB (10 μM) upon addition of H_2O_2 in DMSO-PBS buffer solution (10.0 mM, pH = 7.4, 1:1, *v/v*). λex = 561 nm, slit: 5 nm/5 nm. d SIM images of HeLa cells stained with MDBRe (10 μM) for 1 h. e Representative fluorescence intensity of MDBRe (green line) and PKMTDR (red line) in the mitochondrial region. f Schematic diagram of the morphology of mitochondrial damage caused by 1% NaN_3. g SIM images of mitochondrial damage in cells treated with 1% NaN_3 for 3 h and PKMTDR (λex = 640 nm) for 20 min. h The definition of L/W parameters for the description of mitochondrial morphology description. i Quantitative analysis of mitochondria in the control, NaN_3-treated group, and the experimental group treated with MDB (10 μM) for 1 h. (Data are mean ± SEM. n s, no significant difference, $^{*}P < 0.05$, $^{**}P < 0.01$, $^{***}P < 0.001$). (For interpretation of the references to colour in this figure legend, the reader is referred to the web version of this article.)

suggesting that MDBRe binding to HO-1 could impact its activity. To determine the affinity between MDBRe and HO-1 accurately, we examined their interaction using MicroScale Thermophoresis (MST). Through titrating solutions of HO-1 at various concentrations with a constant 1 mM concentration of MDBRe, as depicted in Fig. S15, we calculated a dissociation coefficient of Kd = 236.7 nM, indicating a strong binding affinity between MDBRe and HO-1. This experiment illustrated that MDBRe could bind to HO-1, potentially influencing the function and activity of HO-1 within cells. Additionally, we observed a π-π interaction between the benzene ring of the MDBRe molecule and the heme substrate (Fig. 1b, right diagram), suggesting that MDBRe may inhibit HO-1 function by forming a stable complex.

3.2. Prodrug MDB release beacon drug MDBRe in HeLa cells

Next, the potential of MDB as a beacon drug delivery system in live cells was further investigated. Initially, the cytotoxicity of MDB in HeLa cells was assessed using the CCK-8 assay. Results depicted in Fig. S16 indicated that at a concentration of 5 μM, MDB had negligible cytotoxic effects on HeLa cells over 24 h; however, at 10 μM, cell survival rates began to decrease. To enable cellular studies without compromising drug efficacy or cell viability, 10 μM was selected as the optimal concentration of MDB for super-resolution imaging in live cells. Employing SIM, we observed that prodrug MDB displayed excellent mitochondrial targeting ability and was subsequently activated by intracellular H_2O_2 to release the drug MDBRe (Fig. 2a and b; green in the picture). Interestingly, while MDBRe was co-stained with the mitochondrial probe, it did not exhibit mitochondrial localization ability (Fig. 2d and e), indicating the remarkable targeting properties of boronate. SIM imaging results revealed the initial accumulation of the prodrug MDB on the mitochondria (labeled with PKMTDR and represented by red fluorescence) upon cell entry, followed by activation by mitochondrial H_2O_2, resulting in the release of the beacon drug MDBRe (Fig. 2a and b; displayed as green fluorescence). Notably, direct incubation of cells with MDBRe showed no localization to the mitochondria (Fig. 2d and e), suggesting that the borate ester group within the prodrug MDB directed its mitochondrial localization, enabling a response to mitochondrial H_2O_2 and facilitating the release of the beacon drug MDBRe. It is notable that incubation with MDBRe or MDB induced changes in the morphology of mitochondria in the cells, resulting in a short rod or circular shape (Fig. 2a and d). This observation led us to consider the possibility of mitochondrial damage caused by the drug. To investigate further, we compared the effects of MDB treatment with mitochondrial damage induced by 1% NaN_3 [37]. In cells treated with NaN_3, the mitochondrial morphology shifted from a normal filamentous form (Fig. S17) to a short rod-like or nearly circular shape (Fig. 2f and g). The similarity in mitochondrial morphology alterations between the MDB-treated and NaN_3-treated groups indicates substantial mitochondrial damage. Subsequently, we employed the classical method $-L/W$ to quantitatively assess mitochondrial morphology in these groups: a ratio of $1.0 \leq L/W < 1.5$ for round shapes, $1.5 \leq L/W < 2.0$ for intermediate shapes, $2.0 \leq L/W < 5.0$ for tubular shapes, and $L/W \geq 5.0$ for hyperfused appearances (Fig. 2h). Analysis of the results revealed comparable levels of mitochondrial damage between those subjected to MDB and NaN_3 treatment (Fig. 2i). In conclusion, this study illustrates the ability of MDB to target the mitochondria of tumor cells and, upon response to H_2O_2, release the beacon drug MDBRe, consequently leading to mitochondrial structural damage.

3.3. The beacon drug MDBRe results in mitochondrial damage, leading to the apoptosis of tumor cells

We further investigated the specific mechanism of mitochondrial damage caused by MDB. Cells treated with MDB were co-labelled with heme oxygenase-1 (HO-1) and a mitochondrial fluorescence probe, then observed using SIM. Results demonstrated that MDB released MDBRe (green fluorescence) at the mitochondria, which diffused and co-localized with HO-1 (blue fluorescence), leading to significant mitochondrial damage (Fig. 3a and b). To confirm that mitochondrial damage was due to MDBRe and not the prodrug MDB, cells were pre-treated with acetovanillone to reduce the overproduction of ROS [38]. This led to a visible normal mitochondrial morphology and a reduction in damaged mitochondria (Fig. 3e and f), in contrast to the notable mitochondrial damage observed in cells treated with MDBRe (Fig. 3c and d). To prevent the release of MDBRe, cells were treated with oxyresveratrol, known for its antioxidant and free-radical scavenging properties [39]. Subsequent treatment with the prodrug MDB revealed mitochondrial structures displaying fibrous and rod-shaped characteristics, suggesting minimal mitochondrial damage in the imaging results (Fig. 3g and h). At the same time, the mitochondrial membrane potential of the HeLa cells was measured by JC-1. The results showed that JC-1 probe exhibited stronger red fluorescence after incubation with Oxyresveratrol for 12 h, while it showed enhanced green fluorescence after direct incubation with MDBRe (Figs. S18 and S19), which is consistent with the degree of mitochondrial damage revealed in SIM imaging. Taken together, The prodrug MDB itself showed no effect on mitochondria; however, increased intracellular H_2O_2 levels triggered its conversion into MDBRe, leading to mitochondrial damage and an elevation in intracellular ROS levels. Subsequent incubation with MDB led to a significant increase in ROS levels over 30 min (Fig. S20, Fig. 3i and j), reinforcing the activation of the prodrug MDB, thus establishing a synergistic effect enhancing the efficacy of the beacon drugs. Flow cytometry was used to assess the impact of MDB on HeLa cell apoptosis post 24-hour exposure to 0, 10, 20, and 30 μM MDB concentrations. The results demonstrated a gradual increase in the apoptosis rate of HeLa cells with higher MDB concentrations, showing rates of 0.05 %, 11.98 %, 25.70 %, and 39.62 %, respectively (Fig. 3k, Fig. S21). These findings underline the potent anti-tumor effect of the beacon drug. Additionally, apoptotic analysis using confocal fluorescence microscopy further supported the tumor cell apoptosis induced by MDB incubation (Fig. S22).

We conducted a further investigation to determine the impact of MDB on normal cells where ROS production is tightly controlled [40]. Three normal cell lines, AT3, H9c2, and L929 were analyzed using SIM and cell viability studies. SIM imaging revealed only minimal fluorescence of MDB in the cells, with the mitochondrial maintaining their normal fiber or rod-like structures. This observation indicated that MDB did not have a toxic effect on normal cells (Figs. S23a, S24a, S25a). Consistently, cell viability results corroborated these findings (Figs. S23b, S24b, S25b). These studies demonstrated that a high expression of H_2O_2 was necessary for the activation of prodrug MDB. In the absence of excess H_2O_2, MDB did not induce cellular damage. In summary, the prodrug MDB is selectively activated within tumor cells to release the beacon drug MDBRe, thereby triggering tumor cell apoptosis. Importantly, this effect is not observed in normal cells.

3.4. The anti-tumor activity of the prodrug MDB in mouse models

Encouraged by the promising *in vitro* results, we established a tumor-bearing Nude mouse model to assess the anti-tumor efficacy of MDB *in vivo*. Twenty tumor-bearing mice were randomly assigned to four groups (n = 5), receiving varying doses of MDB injected into the tumor sites every 2 days (Fig. 4a). We monitored tumor growth by measuring changes in tumor volume and weight over time. Interestingly, mice treated with a 30 μM dosage exhibited the slowest tumor growth, the smallest tumor volume, and the greatest tumor inhibition rate compared to the PBS controls (Fig. 4b–d, Fig. S26). In contrast, the body weight of the mice exhibited minimal fluctuations (Fig. S27). However, mice receiving a 10 μM dosage showed larger tumor volume and weight than the control group, contrary to the *in vitro* findings. This disparity may be attributed to the hormetic of the anti-tumor drug, where drugs exhibit a stimulating effect on biological systems at low doses and an inhibitory effect at high doses [41,42]. To confirm the stimulatory effect of MDB,

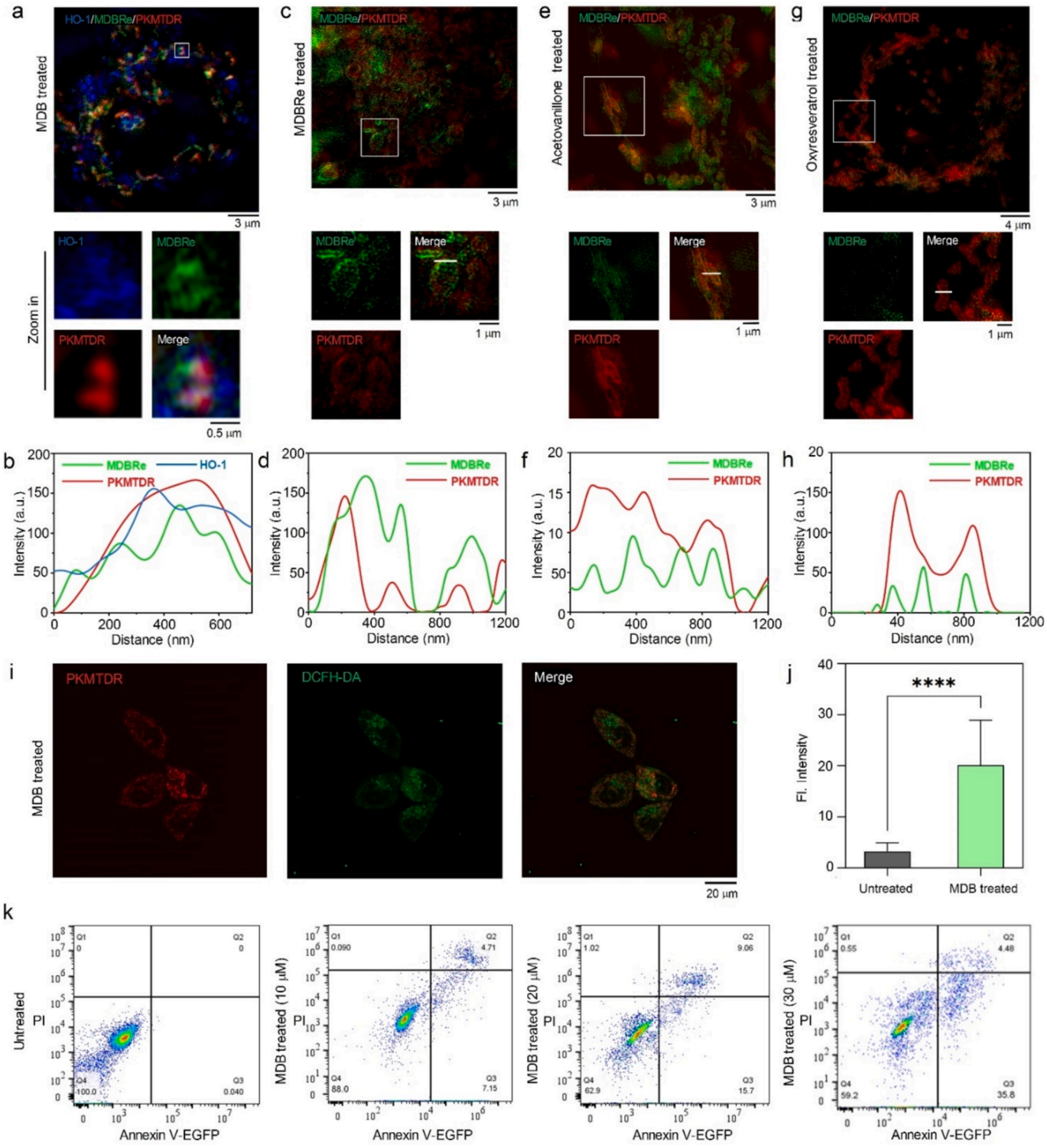

Fig.3. Beacon drug MDBRe results in mitochondrial damage in HeLa cells. a SIM images of HeLa cells stained with HO-1 and MDB (10 μM) for 1 h. c SIM images of HeLa cells stained with MDBRe (10 μM) for 1 h. e SIM images of HeLa cells stained ROS inhibitor Acetovanillone (10 μM) for 12 h and incubated with prodrug MDB (10 μM) for 1 h. g SIM images of mitochondria after treating H_2O_2 scavenger Oxyresveratrol (50 μM) for 12 h and incubated with prodrug MDB (10 μM) for 1 h. b d f h The fluorescence intensity of MDBRe (green line) and PKMTDR (red line) in white line from a, c, e and g, respectively. (MDBRe: λex = 561 nm; PKMTDR, λex = 640 nm) i Detection of ROS production using ROS Assay Kit (DCFH-DA, 10 μM) in HeLa cells with 10 μM MDB treated. The greener the cells, the more ROS it is. Green channel: λex = 488 nm, λem = 525 nm; Red channel: λex = 640 nm. j ROS quantitative analysis in normal and MDB (10 μM) treated groups. k Annexin V-EGFP/PI flow cytometry analysis of HeLa cells treated with 0, 10, 20, and 30 μM of MDB for 24 h. Annexin V-EGFP, λex = 488 nm, λem = 507 nm. PI, λex = 488 nm, λem = 695 nm. (For interpretation of the references to colour in this figure legend, the reader is referred to the web version of this article.)

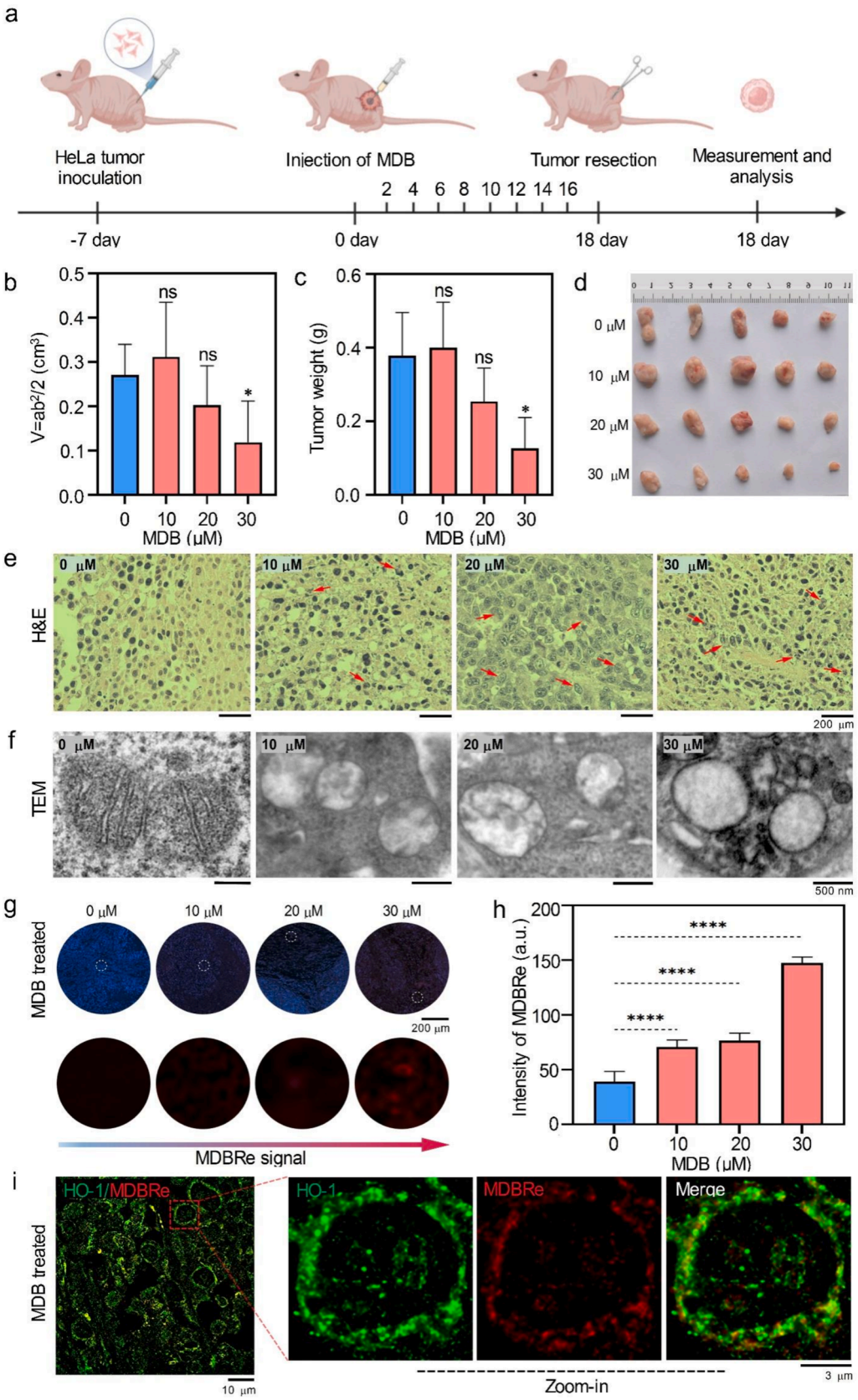

(caption on next page)

Fig.4. *In vivo* anti-tumor effects in HeLa-cell-derived tumor xenograft model. a Schematic illustration of MDB for anticancer therapy for HeLa primary tumors. The drug concentration was 0, 10, 20, and 30 μM, respectively. b c The tumor volume and weights of tumor-bearing mice were measured after 18-days of treatment. The tumor xenograft volume was calculated using the following formula: $V = ab^2/2$ (a: the long diameter and b: the short diameter). Datas as shown as mean ± SEM (n = 5). $^*p < 0.05$, $^{**}p < 0.01$, $^{***}p < 0.001$. d Photograph of tumors after excision from each group. e Hematoxylin and eosin (H&E) staining images of tumors in different groups. f TEM ultrathin sectioning images of mitochondrial morphology in different groups. g The *in situ* slice imaging of DAPI (λex = 340 nm) and MDBRe (λex = 561 nm) staining of the tumors when treated with different concentrations of MDB. Zoom-in images of regions of interest are presented in white rectangles. h Quantitative analysis of MDBRe fluorescence intensity in tumor sections after the tumors were treated with different concentrations of MDB. i The *in situ* slice SIM imaging of HO-1 (λex = 405 nm) and MDBRe (λex = 561 nm) staining of the tumors when treated with different concentrations of MDB. Zoom-in images of regions of interest are presented in white rectangles.

we used low doses of MDB to incubate HeLa cells. The results showed that MDB at low concentrations can promote cell proliferation (Fig. S28). *Ex vivo* tumor imaging revealed significantly enhanced fluorescent signals (Inset, Fig. S29), and *in vivo* imaging of mice revealed distinct fluorescence signals of drug molecule MDBRe at the tumor site, with weaker fluorescence signals surrounding the tumor (Fig. S29). This observation could be linked to localized inflammation around the tumor, which is also associated with high levels of ROS expression [43,44]. In addition, *ex vivo* imaging of major organs showed intensified fluorescent signals specifically at the tumor site, which is attributed to the activation of MDB by H_2O_2 in TME and releasing MDBRe, while the liver and kidneys had weaker signals, possibly due to partial MDBRe being metabolized to the liver and kidneys (Fig. S30). Analysis of hematoxylin-eosin (H&E)-stained images of tumor sections showed tumor cells exhibited round in morphology and pyknotic nuclei after treatment with MDB compared to the control group (Fig. 4e). Additionally, ultrathin sections of tumor after drug treatment were observed by transmission electron microscope (TEM) imaging, which showed mitochondrial morphology changed to nearly round shape in MDB-treated cells, comparing to the filamentous arrangement in an irregular manner of the untreated group (Fig. 4f). Evaluation of *in situ* apoptosis within the tumor tissue using TUNEL staining revealed an increase in green fluorescence indicative of apoptosis with rising MDB concentration, suggesting drug-dependent apoptosis in the treated tumors (Figs. S31–33). The activation of the beacon drug MDBRe, triggered by elevated levels of H_2O_2 within the TME, was confirmed through *in situ* slice imaging displaying red fluorescence signals in the tumors (Fig. 4g and h). 3D imaging of tumor *in situ* also demonstrated that MDBRe has excellent capability for tumor imaging (Fig. S34). The results from SIM imaging of *in situ* tumor sections demonstrated a substantial colocalization of MDBRe with HO-1(Fig. 4i), reinforcing the localization and activation of the prodrug within the tumor area and its role in inducing mitochondrial damage and tumor cell apoptosis *in vivo*.

Finally, the main organs (heart, liver, spleen, lung, and kidney) of the MDB-treated mice were collected at 18-day time points post-injection to evaluate the possible side effects. The histological analysis toward the main organs exhibited normal pathologic morphology with negligible damage (Fig. S35). The hemolysis and routine blood test revealed that MDBRe had excellent biocompatibility (Figs. S36 and S37).

3.5. Alterations in cellular proteomic expression induced by MDB treatment

Oxidative stress and mitochondrial damage are widely acknowledged to result in the excessive production of ROS, which is a primary cause of tissue injury associated with inflammation [45,46]. Various well-known inflammatory proteins, such as COX-2, have been associated with oxidative stress and ROS generation [47,48]. To investigate the impact of this, HeLa cells were treated with different concentrations of MDB, following which western blotting experiments were conducted. The finding revealed increased COX-2 expression levels, indicating that mitochondrial damage could induce oxidative stress and inflammatory responses (Fig. 5a–c). To delve deeper into MDB's mechanism of action, proteomic profiling experiments were carried out to quantify and assess protein levels in HeLa cells pre and post MDB treatment. A total of 6013 quantifiable proteins were identified (Fig. S38), and a T-test was performed to evaluate the significance of protein levels pre and post-treatment. A default *P*-value of < 0.05 was set, with a fold change threshold of 1.2 for upregulation, and 1/1.2 for down-regulation. Results showed a significant difference in protein levels, in samples treated with 10 μM of MDB compared to the PBS control group, with 66 proteins up-regulated and 60 down-regulated (Fig. 5d and e). Notably, amongst the proteins showing significant alterations, 11.9 % were mitochondria, 27.78 % were nucleus, and 19.84 % cytoplasm (Fig. 5f). A key observation was the downregulation of HO-1 in peroxisomes, typically upregulated in response to elevated ROS [49–51] but reversed by MDBRe, indicating that MDBRe has a direct inhibitory effect on HO-1 (Fig. 5g and h). This aligns with immunofluorescence findings demonstrating reduced HO-1 expression in tumor tissues, suggesting that MDB could impact cancer cell viability by inducing HO-1 downregulation, mitochondrial damage, and apoptotic effects (Fig. 5j, i, Fig. S39). To explore additional processes involved, Gene Ontology (GO) classification and Kyoto Encyclopedia of Genes Genomes (KEGG) annotation were employed to further dissect the functions of the impacted proteins. The results showed that MDB significantly influenced neutrophil aggregation, extracellular matrix assembly, and chemokine production (Fig. 5k). Consequently, MDB could lead to tissue damage and provoke an anti-inflammatory response. Furthermore, there was a substantial alteration in the regulation of the apoptotic process and programmed cell death, facilitating the metabolic death of cancer cells. Additionally, several signaling pathways linked to cancer were up-regulated, such as those related to inflammatory bowel disease and cytokine-cytokine receptor interaction (Fig. 5l). These pathways were further stimulated following MDB treatment, consequently heightening the probability of cell death. In summary, proteomic analysis demonstrated that MDB treatment induced proteomic alterations consistent with its known effects on apoptosis, tumor signaling, and mitochondrial damage.

4. Conclusion

Here, we proposed a strategy for the development of a beacon drug delivery system. This system enables the TME-targeted release of the designed beacon drug MDBRe from prodrug MDB. The prodrug MDB contains a boronate ester group that facilitates its accumulation in mitochondria and responsiveness to the high levels of H_2O_2 present in tumor cells, leading to the release of the visualizable beacon drug MDBRe. Importantly, MDBRe is minimally released in normal cells due to their low H_2O_2 expression, thereby displaying no cytotoxic effects. Super-resolution imaging confirmed the release of MDBRe following MDB incubation in tumor cells, resulting in mitochondrial damage through HO-1 inhibition, leading to increased ROS levels and apoptotic induction. The proteomic analysis also indicated that MDBRe induced mitochondrial dysfunction by influencing HO-1 expression. This beacon drug delivery system enables us to accurately deliver beacon drugs to tumor sites, visualizing the activation process *in vivo* and elucidating how beacon drugs effectively inhibit tumor growth while minimizing normal tissue side effects. Ultimately, this system presents a promising strategy for the development of more effective anti-tumor drugs.

CRediT authorship contribution statement

Yongchun Wei: Writing – review & editing, Writing – original draft,

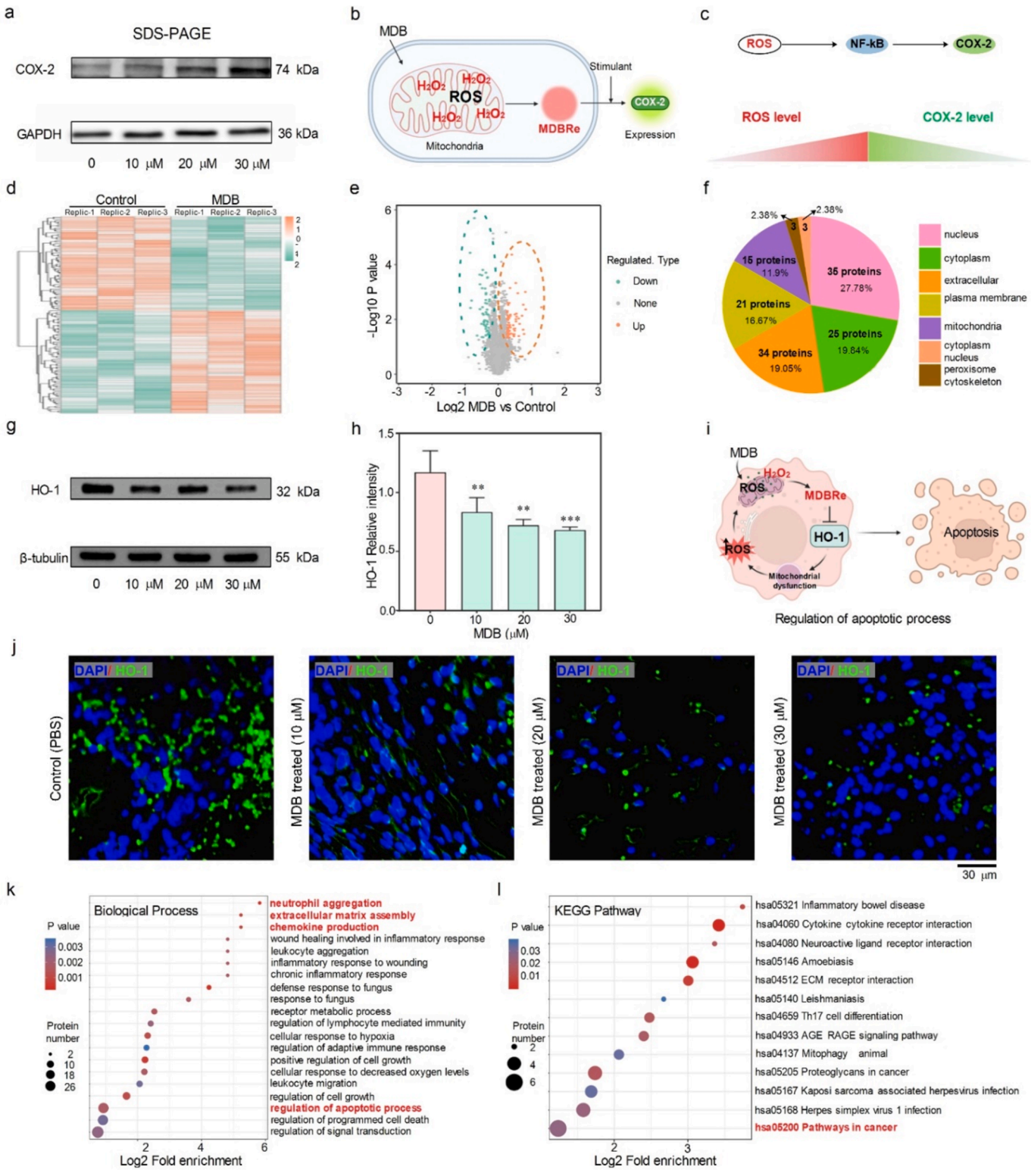

Fig.5. Proteomics analysis of HeLa cells treated with prodrug MDB. a The expression of ROS-related proteins (COX-2) was analyzed using Western blotting. b Schematic illustration of prodrug-stimulated protein COX-2 expression. c Schematic diagram of the relationship between ROS level and COX-2 expression level. d Heatmap cluster of proteomic changes before and after MDB (10 μM) treatment for 1 h in HeLa cells. e Volcanic map of proteomic changes before or after MDB (10 μM) treatment for 1 h. f Subcellular localization of proteins that have differentially expression after MDB (10 μM) treatment for 1 h. g Western blot of downregulated protein HO-1 in different groups. h Quantitative statistical analysis of the expression of HO-1 protein relative to internal reference protein β-tubulin. Data are mean ± SEM. Statistical differences are presented $^{*}P < 0.05$, $^{**}P < 0.01$, $^{***}P < 0.001$. i Schematic diagram of the regulation of the apoptotic process by prodrug MDB. j Immunofluorescence staining images of the dissected tumor tissues after 18 days of treatment. (DAPI, blue, λex = 340 nm; HO-1, green, λex = 488 nm) k Gene Ontology (GO) analysis of changed proteins after MDB (10 μM) treatment for 1 h. l The analysis of KEGG pathways of changed proteins after MDB (10 μM) treatment for 1 h. (For interpretation of the references to colour in this figure legend, the reader is referred to the web version of this article.)

Valid, ation, Investigation, Formal analysis, Data curation. **Jiaqi Xing:** Validation, Data curation. **Jiarao Sun:** Validation, Data curation. **Wei Chen:** Validation, Data curation. **Gongchang Yu:** Data curation. **Bin Shi:** Writing – review & editing, Conceptualization. **Xintian Shao:** Writing – review & editing, Supervision, Funding acquisition, Conceptualization. **Yanfeng Wang:** Writing – review & editing, Supervision, Funding acquisition, Conceptualization.

Declaration of competing interest

The authors declare the following financial interests/personal relationships which may be considered as potential competing interests: **Yanfeng Wang, Xintian Shao,** and **Bin Shi** contributed to the design of the experiments; **Yongchun Wei** synthesized and characterized prodrug and contributed to molecular docking simulation; **Jiarao Sun and Wei Chen** cultured cells; **Jiaqi Xing, Jiarao Sun** and **Yongchun Wei** collected all 3D-SIM super-resolution microscopy data; **Yongchun Wei** and **Jiarao Sun** analyzed and processed the SIM data; **Yongchun Wei, Jiaqi Xing, Jiarao Sun** and **Wei Chen** were in charge of the animal studies; **Yongchun Wei, Gongchang Yu, Xintian Shao** and **Yanfeng Wang** contributed to writing the manuscript with the help of all authors.

Acknowledgments

This work was financially supported by the National Natural Science Foundation of China (Nos.82302743), Natural Science Foundation of Shandong Province (ZR2022QH304), National Administration of Traditional Chinese Medicine-Shandong Province Joint Construction of Traditional Chinese Medicine Technology Project (GZY-KJS-SD-2023-085), Shandong Province Traditional Chinese Medicine Science and Technology Project (Q-2023059), Shandong Provincial Central Government Guides Local Science and Technology Development Fund Project (YDZX20203700002055), the project of Haixi Science and Technology Bureau of Qinghai Province (2017-Q4), and the Academic Promotion Program of Shandong First Medical University (Nos.2019LJ003). Some images were created by the authors using BioRender.com.

Appendix A. Supplementary data

Supplementary data to this article can be found online at https://doi.org/10.1016/j.cej.2024.156923.

Data availability

No data was used for the research described in the article.

References

[1] W. Zhen, S. An, S. Wang, W. Hu, Y. Li, X. Jiang, J. Li, Precise subcellular organelle targeting for boosting endogenous-stimuli-mediated tumor therapy, Adv. Mater. 33 (51) (2021), https://doi.org/10.1002/adma.202101572.
[2] J. Yang, A. Griffin, Z. Qiang, J. Ren, Organelle-targeted therapies: a comprehensive review on system design for enabling precision oncology, Signal Transduct. Target. Ther. 7 (1) (2022), https://doi.org/10.1038/s41392-022-01243-0.
[3] F. Kong, C. Wang, L. Zhao, D. Liao, X. Wang, B. Sun, P. Yang, Y. Jia, Traditional Chinese medicines for non-small cell lung cancer: therapies and mechanisms, Chinese Herbal Med. 15 (4) (2023) 509–515, https://doi.org/10.1016/j.chmed.2023.05.004.
[4] S. Bolisetty, A. Traylor, A. Zarjou, M.S. Johnson, G.A. Benavides, K. Ricart, R. Boddu, R.D. Moore, A. Landar, S. Barnes, V. Darley-Usmar, A. Agarwal, Mitochondria-targeted heme oxygenase-1 decreases oxidative stress in renal epithelial cells, Am. J. Physiol. Renal Physiol. 305 (3) (2013) F255–F264, https://doi.org/10.1152/ajprenal.00160.2013.
[5] H.B. Li, X.Z. Zhang, Y. Sun, Q. Zhou, J.N. Song, Z.F. Hu, Y. Li, J.N. Wu, Y. Guo, Y. Zhang, J. Shi, J.B. Yu, HO-1/PINK1 regulated mitochondrial fusion/fission to inhibit pyroptosis and attenuate septic acute kidney injury, Biomed Res. Int. 2020 (2020) 2148706, https://doi.org/10.1155/2020/2148706.
[6] T.D. Hull, R. Boddu, L. Guo, C.C. Tisher, A.M. Traylor, B. Patel, R. Joseph, S. D. Prabhu, H.B. Suliman, C.A. Piantadosi, A. Agarwal, J.F. George, Heme oxygenase-1 regulates mitochondrial quality control in the heart, JCI Insight 1 (2) (2016) e85817, https://doi.org/10.1172/jci.insight.85817.
[7] A.N. Fallica, V. Sorrenti, A.G. D'Amico, L. Salerno, G. Romeo, S. Intagliata, V. Consoli, G. Floresta, A. Rescifina, V. D'Agata, L. Vanella, V. Pittalà, Discovery of novel acetamide-based heme oxygenase-1 inhibitors with potent in vitro antiproliferative activity, J. Med. Chem. 64 (18) (2021) 13373–13393, https://doi.org/10.1021/acs.jmedchem.1c00633.
[8] A. Loboda, A. Jozkowicz, J. Dulak, HO-1/CO system in tumor growth, angiogenesis and metabolism – targeting HO-1 as an anti-tumor therapy, Vasc. Pharmacol. 74 (2015) 11–22, https://doi.org/10.1016/j.vph.2015.09.004.
[9] M.T. Do, H.G. Kim, T. Khanal, J.H. Choi, D.H. Kim, T.C. Jeong, H.G. Jeong, Metformin inhibits heme oxygenase-1 expression in cancer cells through inactivation of Raf-ERK-Nrf2 signaling and AMPK-independent pathways, Toxicol. Appl. Pharmacol. 271 (2) (2013) 229–238, https://doi.org/10.1016/j.taap.2013.05.010.
[10] L. Salerno, G. Romeo, M.N. Modica, E. Amata, V. Sorrenti, I. Barbagallo, V. Pittala, Heme oxygenase-1: a new druggable target in the management of chronic and acute myeloid leukemia, Eur. J. Med. Chem. 142 (2017) 163–178, https://doi.org/10.1016/j.ejmech.2017.07.031.
[11] S. Schulz, R.J. Wong, H.J. Vreman, D.K. Stevenson, Metalloporphyrins – an update, Front. Pharmacol. 3 (2012) 68, https://doi.org/10.3389/fphar.2012.00068.
[12] K.F. Greish, L. Salerno, R. Al Zahrani, E. Amata, M.N. Modica, G. Romeo, A. Marrazzo, O. Prezzavento, V. Sorrenti, A. Rescifina, G. Floresta, S. Intagliata, V. Pittala, Novel structural insight into inhibitors of heme oxygenase-1 (HO-1) by new imidazole-based compounds: biochemical and in vitro anticancer activity evaluation, Molecules 23 (5) (2018), https://doi.org/10.3390/molecules23051209.
[13] S.K. Chiang, S.E. Chen, L.C. Chang, A dual role of heme oxygenase-1 in cancer cells, Int. J. Mol. Sci. 20 (1) (2018), https://doi.org/10.3390/ijms20010039.
[14] X. Wei, X. Chen, M. Ying, W. Lu, Brain tumor-targeted drug delivery strategies, Acta Pharm. Sin. B 4 (3) (2014) 193–201, https://doi.org/10.1016/j.apsb.2014.03.001.
[15] D. Rosenblum, N. Joshi, W. Tao, J.M. Karp, D. Peer, Progress and challenges towards targeted delivery of cancer therapeutics, Nat. Commun. 9 (1) (2018) 1410, https://doi.org/10.1038/s41467-018-03705-y.
[16] D.E. Large, J.R. Soucy, J. Hebert, D.T. Auguste, Advances in receptor-mediated, tumor-targeted drug delivery, Adv. Therap. 2 (1) (2019), https://doi.org/10.1002/adtp.201800091.
[17] S. Prasad, S.C. Gupta, A.K. Tyagi, Reactive oxygen species (ROS) and cancer: role of antioxidative nutraceuticals, Cancer Lett. 387 (2017) 95–105, https://doi.org/10.1016/j.canlet.2016.03.042.
[18] A. Costa, A. Scholer-Dahirel, F. Mechta-Grigoriou, The role of reactive oxygen species and metabolism on cancer cells and their microenvironment, Semin. Cancer Biol. 25 (2014) 23–32, https://doi.org/10.1016/j.semcancer.2013.12.007.
[19] L. Zhong, Y. Li, L. Xiong, W. Wang, M. Wu, T. Yuan, W. Yang, C. Tian, Z. Miao, T. Wang, S. Yang, Small molecules in targeted cancer therapy: advances, challenges, and future perspectives, Signal Transduct. Target. Ther. 6 (1) (2021) 201, https://doi.org/10.1038/s41392-021-00572-w.
[20] P.L. Bedard, D.M. Hyman, M.S. Davids, L.L. Siu, Small molecules, big impact: 20 years of targeted therapy in oncology, Lancet 395 (10229) (2020) 1078–1088, https://doi.org/10.1016/S0140-6736(20)30164-1.
[21] Y. Wu, H. Shroff, Faster, sharper, and deeper: structured illumination microscopy for biological imaging, Nat. Methods 15 (12) (2018) 1011–1019, https://doi.org/10.1038/s41592-018-0211-z.
[22] Q. Chen, H. Fang, X. Shao, Z. Tian, S. Geng, Y. Zhang, H. Fan, P. Xiang, J. Zhang, X. Tian, K. Zhang, W. He, Z. Guo, J. Diao, A dual-labeling probe to track functional mitochondria-lysosome interactions in live cells, Nat. Commun. 11 (1) (2020) 6290, https://doi.org/10.1038/s41467-020-20067-6.
[23] Y. Wei, L. Kong, H. Chen, Y. Liu, Y. Xu, H. Wang, G. Fang, X. Shao, F. Liu, Y. Wang, Q. Chen, Super-resolution image-based tracking of drug distribution in mitochondria of a label-free naturally derived drug molecules, Chem. Eng. J. 429 (2022), https://doi.org/10.1016/j.cej.2021.132134.
[24] R. Heintzmann, T. Huser, Super-resolution structured illumination microscopy, Chem. Rev. 117 (23) (2017) 13890–13908, https://doi.org/10.1021/acs.chemrev.7b00218.
[25] W. Lang, C. Yuan, L. Zhu, S. Du, L. Qian, J. Ge, S.Q. Yao, Recent advances in construction of small molecule-based fluorophore-drug conjugates, J. Pharm. Anal. 10 (5) (2020) 434–443, https://doi.org/10.1016/j.jpha.2020.08.006.
[26] A. Zhang, K. Meng, Y. Liu, Y. Pan, W. Qu, D. Chen, S. Xie, Absorption, distribution, metabolism, and excretion of nanocarriers in vivo and their influences, Adv. Colloid Interface Sci. 284 (2020) 102261, https://doi.org/10.1016/j.cis.2020.102261.
[27] J.B. Baell, J.W.M. Nissink, Seven year itch: pan-assay interference compounds (PAINS) in 2017-utility and limitations, ACS Chem. Biol. 13 (1) (2018) 36–44, https://doi.org/10.1021/acschembio.7b00903.
[28] L.Y. Chau, Heme oxygenase-1: emerging target of cancer therapy, J. Biomed. Sci. 22 (1) (2015) 22, https://doi.org/10.1186/s12929-015-0128-0.
[29] M. Nitti, S. Piras, U.M. Marinari, L. Moretta, M.A. Pronzato, A.L. Furfaro, HO-1 induction in cancer progression: a matter of cell adaptation, Antioxidants (basel) 6 (2) (2017), https://doi.org/10.3390/antiox6020029.
[30] K.N. Luu Hoang, J.E. Anstee, J.N. Arnold, The diverse roles of heme oxygenase-1 in tumor progression, Front. Immunol. 12 (2021) 658315, https://doi.org/10.3389/fimmu.2021.658315.
[31] Z. Zhuang, Q. Yang, Z. Zhang, Q. Zhang, G. Zheng, F. Zhan, A highly selective fluorescent probe for hydrogen peroxide and its applications in living cells,

J. Photochem. Photobiol. A Chem. 344 (2017) 8–14, https://doi.org/10.1016/j.jphotochem.2017.04.009.
[32] L. Lad, D.J. Schuller, H. Shimizu, J. Friedman, H. Li, P.R. Ortiz de Montellano, T. L. Poulos, Comparison of the heme-free and -bound crystal structures of human heme oxygenase-1, J. Biol. Chem. 278 (10) (2003) 7834–7843, https://doi.org/10.1074/jbc.M211450200.
[33] L.H. Fu, Y. Wan, C. Qi, J. He, C. Li, C. Yang, H. Xu, J. Lin, P. Huang, Nanocatalytic theranostics with glutathione depletion and enhanced reactive oxygen species generation for efficient cancer therapy, Adv. Mater. 33 (7) (2021), https://doi.org/10.1002/adma.202006892.
[34] J. Chen, Y. Zhu, Y. Zhang, Glutathione-capped Mn-doped ZnS quantum dots as a room-temperature phosphorescence sensor for the detection of Pb(2+) ions, Spectrochim. Acta A Mol. Biomol. Spectrosc. 164 (2016) 98–102, https://doi.org/10.1016/j.saa.2016.04.014.
[35] G. Bauer, The synergistic effect between hydrogen peroxide and nitrite, two long-lived molecular species from cold atmospheric plasma, triggers tumor cells to induce their own cell death, Redox Biol. 26 (2019) 101291, https://doi.org/10.1016/j.redox.2019.101291.
[36] Y. Wang, X. Yang, X. Chen, X. Wang, Y. Wang, H. Wang, Z. Chen, D. Cao, L. Yu, J. Ding, Sustained release of nitric oxide and cascade generation of reactive nitrogen/oxygen species via an injectable hydrogel for tumor synergistic therapy, Adv. Funct. Mater. 32 (36) (2022), https://doi.org/10.1002/adfm.202206554.
[37] H. Lecoeur, L.M. de Oliveira-Pinto, M.L. Gougeon, Multiparametric flow cytometric analysis of biochemical and functional events associated with apoptosis and oncosis using the 7-aminoactinomycin D assay, J. Immunol. Methods 265 (1–2) (2002) 81–96, https://doi.org/10.1016/s0022-1759(02)00072-8.
[38] E.H.M. Hassanein, O.A.M. Abd El-Ghafar, M.A. Ahmed, A.M. Sayed, W.M. Gad-Elrab, J.S. Ajarem, A.A. Allam, A.M. Mahmoud, Edaravone and acetovanillone upregulate Nrf2 and PI3K/Akt/mTOR signaling and prevent cyclophosphamide cardiotoxicity in rats, Drug Des. Devel. Ther. 14 (2020) 5275–5288, https://doi.org/10.2147/DDDT.S281854.
[39] P. Lorenz, S. Roychowdhury, M. Engelmann, G. Wolf, T.F. Horn, Oxyresveratrol and resveratrol are potent antioxidants and free radical scavengers: effect on nitrosative and oxidative stress derived from microglial cells, Nitric Oxide 9 (2) (2003) 64–76, https://doi.org/10.1016/j.niox.2003.09.005.
[40] M.N. Sack, F.Y. Fyhrquist, O.J. Saijonmaa, V. Fuster, J.C. Kovacic, Basic biology of oxidative stress and the cardiovascular system: part 1 of a 3-part series, J. Am. Coll. Cardiol. 70 (2) (2017) 196–211, https://doi.org/10.1016/j.jacc.2017.05.034.
[41] A. Gaya, C.A. Akle, S. Mudan, J. Grange, The concept of hormesis in cancer therapy – is less more? Cureus (2015) https://doi.org/10.7759/cureus.261.
[42] E.J. Calabrese, Hormesis is central to toxicology, pharmacology and risk assessment, Hum. Exp. Toxicol. 29 (4) (2010) 249–261, https://doi.org/10.1177/0960327109363973.
[43] Y. Yu, S. Liu, L. Yang, P. Song, Z. Liu, X. Liu, X. Yan, Q. Dong, Roles of reactive oxygen species in inflammation and cancer, MedComm 5 (4) (2024), https://doi.org/10.1002/mco2.519.
[44] W. Zhang, N. Cui, J. Ye, B. Yang, Y. Sun, H. Kuang, Curcumin's prevention of inflammation-driven early gastric cancer and its molecular mechanism, Chin. Herbal Med. 14 (2) (2022) 244–253, https://doi.org/10.1016/j.chmed.2021.11.003.
[45] M. Zhao, Y. Wang, L. Li, S. Liu, C. Wang, Y. Yuan, G. Yang, Y. Chen, J. Cheng, Y. Lu, J. Liu, Mitochondrial ROS promote mitochondrial dysfunction and inflammation in ischemic acute kidney injury by disrupting TFAM-mediated mtDNA maintenance, Theranostics 11 (4) (2021) 1845–1863, https://doi.org/10.7150/thno.50905.
[46] A. Rimessi, M. Previati, F. Nigro, M.R. Wieckowski, P. Pinton, Mitochondrial reactive oxygen species and inflammation: molecular mechanisms, diseases and promising therapies, Int. J. Biochem. Cell Biol. 81 (Pt B) (2016) 281–293, https://doi.org/10.1016/j.biocel.2016.06.015.
[47] M. Munoz, A. Sanchez, M. Pilar Martinez, S. Benedito, M.E. Lopez-Oliva, A. Garcia-Sacristan, M. Hernandez, D. Prieto, COX-2 is involved in vascular oxidative stress and endothelial dysfunction of renal interlobar arteries from obese Zucker rats, Free Radic. Biol. Med. 84 (2015) 77–90, https://doi.org/10.1016/j.freeradbiomed.2015.03.024.
[48] T.P. Liu, Y.P. Chen, C.M. Chou, T.T. Chiu, C.T. Chen, Therapeutic evaluation of HIV transduction basic domain-conjugated superoxide dismutase solution on suppressive effects of the formation of peroxynitrite and expression of COX-2 in murine skin, J. Biomed. Sci. 23 (2016) 11, https://doi.org/10.1186/s12929-016-0226-7.
[49] S. Deng, K. Yu, W. Jiang, Y. Li, S. Wang, Z. Deng, Y. Yao, B. Zhang, G. Liu, Y. Liu, Z. Lian, Over-expression of Toll-like receptor 2 up-regulates heme oxygenase-1 expression and decreases oxidative injury in dairy goats, J. Anim. Sci. Biotechnol. 8 (2017) 3, https://doi.org/10.1186/s40104-016-0136-2.
[50] B. Xu, Y. Qin, D. Li, N. Cai, J. Wu, L. Jiang, L. Jie, Z. Zhou, J. Xu, H. Wang, Inhibition of PDE4 protects neurons against oxygen-glucose deprivation-induced endoplasmic reticulum stress through activation of the Nrf-2/HO-1 pathway, Redox Biol. 28 (2020) 101342, https://doi.org/10.1016/j.redox.2019.101342.
[51] D. Chen, F. Ning, J. Zhang, Y. Tang, X. Teng, NF-κB pathway took part in the development of apoptosis mediated by miR-15a and oxidative stress via mitochondrial pathway in ammonia-treated chicken splenic lymphocytes, Sci. Total Environ. 729 (2020), https://doi.org/10.1016/j.scitotenv.2020.139017.